Zhang *et al. Satellite Navigation* (2022) 3:6
https://doi.org/10.1186/s43020-022-00067-1

Satellite Navigation
https://satellite-navigation.springeropen.com/

ORIGINAL ARTICLE Open Access

Investigating GNSS PPP–RTK with external ionospheric constraints

Xiaohong Zhang[1,2*], Xiaodong Ren[2], Jun Chen[3], Xiang Zuo[4], Dengkui Mei[2] and Wanke Liu[2]

Abstract

Real-Time Kinematic Precise Point Positioning (PPP–RTK) is inextricably linked to external ionospheric information. The PPP–RTK performances vary much with the accuracy of ionospheric information, which is derived from different network scales, given different prior variances, and obtained under different disturbed ionospheric conditions. This study investigates the relationships between the PPP–RTK performances, in terms of precision and convergence time, and the accuracy of external ionospheric information. The statistical results show that The Time to First Fix (TTFF) for the PPP–RTK constrained by Global Ionosphere Map (PPP–RTK-GIM) is about 8–10 min, improved by 20%–50% as compared with that for PPP Ambiguity Resolution (PPP-AR) whose TTFF is about 13–16 min. Additionally, the TTFF of PPP–RTK is 4.4 min, 5.2 min, and 6.8 min, respectively, when constrained by the external ionospheric information derived from different network scales, e.g. small-, medium-, and large-scale networks, respectively. To analyze the influences of the optimal prior variances of external ionospheric delay on the PPP–RTK results, the errors of 0.5 Total Electron Content Unit (TECU), 1 TECU, 3 TECU, and 5 TECU are added to the initial ionospheric delays, respectively. The corresponding convergence time of PPP–RTK is less than 1 min, about 3, 5, and 6 min, respectively. After adding the errors, the ionospheric information with a small variance leads to a long convergence time and that with a larger variance leads to the same convergence time as that of PPP-AR. Only when an optimal prior variance is determined for the ionospheric delay in PPP–RTK model, the convergence time for PPP–RTK can be shorten greatly. The impact of Travelling Ionospheric Disturbance (TID) on the PPP–RTK performances is further studied with simulation. It is found that the TIDs increase the errors of ionospheric corrections, thus affecting the convergence time, positioning accuracy, and reliability of PPP–RTK.

Keywords: GNSS, PPP–RTK, Ionospheric delay information, Ionospheric variance, Convergence time

Introduction

Precise Point Positioning (PPP) can achieve a positioning accuracy of better than 10 cm within 30 min by applying satellite precise orbit and clock products. Much work has been done to reduce the convergence time of PPP, such as using multi-constellation Global Navigation Satellite System (GNSS) data (Guo et al., 2017; Li et al., 2019a, 2019b; Li et al., 2015a; Li et al., 2019c; Lou et al., 2016), performing integer ambiguity resolution (Collins et al., 2008; Ge et al., 2008; Hu et al., 2019; Laurichesse et al., 2009; Li & Zhang, 2012; Li et al., 2016; Liu et al., 2017), and adding priori atmospheric information (de Oliveira et al., 2017). However, it still needs more than 15 min to achieve the solutions with centimeter-level accuracy due to the ambiguity of carrier observations. For the Real-Time Kinematic (RTK) technique, though the ambiguity can be quickly fixed, it cannot be applied by the users far away from the reference stations. PPP–RTK is the integer ambiguity resolution enabled PPP by adding the priori atmospheric information from a local reference network, which has a short convergence time (Wübbena et al., 2005; Li & Zhang et al. 2011; de Oliveira et al., 2017; Zhang et al., 2018). It extends the PPP concept by

*Correspondence: xhzhang@sgg.whu.edu.cn
[1] Chinese Antarctic Center of Surveying and Mapping, Wuhan University, Wuhan 430079, China
Full list of author information is available at the end of the article

providing different kinds of corrections to users, such as satellite orbit, clock, and atmospheric delay corrections as well as satellite phase and code biases. These corrections, when accurately provided, enable regional or even global PPP–RTK users to recover the integer nature of ambiguities, thus improving the positioning accuracy and convergence behavior (Geng et al., 2010; Geng & Shi, 2017; et al., ; 2019; Liu et al., 2017; Li et al., 2019a; Li et al., 2019b; Li et al., 2019c; Zha et al., 2021).

Among all kinds of corrections, the precise ionospheric delay is the main bottleneck limiting the fast and successful ambiguity resolution for PPP–RTK (Hernández-Pajares et al., 2011; Jakowski et al., 2008). Consequently, the precise determination of the ionospheric delay along a specific Line-of-Sight (LoS) and its correction are of great significance for reducing the convergence time of PPP–RTK. Ionospheric delays used for augmenting PPP with Ambiguity Resolution (PPP-AR) are mainly derived with the following two ways. The first one is the two-dimensional vertical thin-shell TEC (Total Electron Content) model established at a specific altitude by using mathematical algorithms, such as spherical harmonics function (Schaer, 1999), spherical cap harmonics function (Haines, 1988; Li et al., 2015b), B-splines, and trigonometric B-splines (Mautz et al., 2005; Schmidt et al., 2008) and so on. Existing studies indicated that benefiting from the vertical ionospheric corrections, the convergence time of PPP–RTK can be reduced (Banville et al., 2014; Psychas et al., 2018). One main problem with the estimated TEC models is the mapping function error. To improve the accuracy of vertical ionospheric TEC model, the ionosphere is divided into many three-dimensional voxels of the same size. Hernández-Pajares et al. (1999) first presented GNSS-based data-driven tomographic models. Since then, many scholars further improved the ionosphere tomographic models by different methods (Wen et al., 2015; Wen et al., 2007, 2008; Zheng et al., 2017, 2018, 2020, 2021). Olivares-Pulido et al. (2019) presented a 4D tomographic ionospheric model to support PPP–RTK, achieving an accuracy better than 10 cm in the horizontal direction within about 10 min. The second one is to interpolate the ionospheric delays with high accuracy derived from networks. It has been demonstrated that PPP–RTK can achieve mm-level positioning accuracy in the horizontal direction by using ionospheric corrections derived from a small-scale network (about dozens of kilometers) (Teunissen et al., 2010; Zhang et al., 2011). Also, the convergence behavior can be significantly improved with TEC in the slant and vertical directions when leveraging a regional network and Global Ionospheric Maps (GIMs) (Xiang et al., 2020). In addition, Wang et al. (2017) found that ten seconds were required to make most of the horizontal positioning errors smaller than 10 cm by using 1 Hz data when the network corrections are provided, such as the satellite clocks, the satellite phase biases, and the ionospheric delays.

Previous studies showed that the convergence time of PPP–RTK can be reduced when constrained by external ionospheric information. However, the performances of PPP–RTK constrained by the ionospheric information, which is derived from different scale networks with different accuracy levels by giving different prior variances, and derived under different ionospheric conditions, are not fully studied. This study addresses the aforementioned problems. The performances of PPP–RTK constrained by different accuracy of ionospheric information for different situations are discussed and analyzed. Finally, summary and conclusions are given.

Methodology

In this section, the algorithms of the PPP–RTK server model, the estimation of ionospheric delay based on carrier phase observations and the PPP–RTK user model are introduced.

PPP–RTK server model

The difference between the observed and calculated observation equations for un-differenced and un-combined at k-th epoch can be described as:

$$\begin{cases} \mathrm{E}(\Delta P^s_{r,i}(k)) = \mathbf{c}^s_r(k)\cdot\Delta\mathbf{x}_r(k) + c\cdot[\mathrm{d}t_r(k) - \mathrm{d}t^s(k)] + g^s_r\cdot T^s_r(k) \\ \qquad\qquad + \mu_i\cdot I^s_{r,i}(k) + B_{r,i} - B^s_i \\ \mathrm{E}(\Delta\Phi^s_{r,i}(k)) = \mathbf{c}^s_r(k)\cdot\Delta\mathbf{x}_r(k) + c\cdot[\mathrm{d}t_r(k) - \mathrm{d}t^s(k)] + g^s_r\cdot T^s_r(k) \\ \qquad\qquad - \mu_i\cdot I^s_{r,i}(k) + b_{r,i} - b^s_i + \lambda_i\cdot N^s_{r,i} \end{cases} \tag{1}$$

where $\mathrm{E}(\cdot)$ denotes the expectation operator; $P^s_{r,i}(k)$ and $\Phi^s_{r,i}(k)$ are the code and phase observations, respectively, from receiver r to satellite s at epoch k for frequency i ($i=1,2$); the 3×1 vector $\Delta\mathbf{x}_r(k)$ denotes the receiver's position increment at epoch k; the 3×1 vector $\mathbf{c}^s_r(k)$ indicates the unit vector from receiver to satellite; c denotes the speed of light in vacuum; $\mathrm{d}t_r$ and $\mathrm{d}t^s$ denote the receiver and satellite clock errors, respectively; $T^s_r(k)$ denotes the zenith non-hydrostatic tropospheric delays

Table 1 The rank deficiencies information, including involved parameters, sizes, and S-basis for PPP–RTK network

Rank deficiency involved parameter	Size	S-basis
dt_r and dt^s	1	dt_p
$B_{r,i}$ and B_i^s	f	$B_{p,i}$
$b_{r,i}$ and b_i^s	f	$b_{p,i}$
$dt_{r\neq p}$, $B_{r\neq p,i}$, and $d_{r\neq p,i}$	n-1	$B_{r\neq p,\mathrm{IF}}$
dt^s, B_i^s, and b_i^s	m	B_{IF}^s
b_i^s and $N_{r,j}^s$	f·m	$N_{p,i}^s$
$b_{r\neq p,i}$ and $N_{r\neq p,i}^s$	f·(n-1)	$N_{r\neq p,i}^q$
T_r^s and dt^s	1	T_p^s
$I_{r,i}^s$, $B_{r\neq p,i}$, and $b_{r\neq p,i}$	n-1	$B_{r\neq p,\mathrm{GF}}$
$I_{r,i}^s$, B_i^s, and b_i^s	m	B_{GF}^s

at epoch k, while the hydrostatic tropospheric delays can be corrected by an empirical model; g_r^s denotes the non-hydrostatic tropospheric mapping function; $B_{r,i}$ and B_i^s are the receiver and satellite code hardware biases, respectively; $b_{r,i}$ and b_i^s are the receiver and satellite carrier phase hardware biases, respectively; $\mu_i = f_1^2/f_i^2$ is the conversion coefficient of ionospheric delay for frequency i; $I_{r,i}^s(k)$ is the first order ionospheric delay for frequency i along a line-of-sight at epoch k; $\lambda_i = c/f_i$ indicates the phase wavelength for frequency i; $N_{r,i}^s$ is the phase integer ambiguity for frequency i.

Equation (1) is a rank deficiency system due to the linear dependency of some columns of the design matrix. To eliminate the rank deficiency, Odijk et al. (2016) proposed the null space of the design matrix and chose a minimum constraint set, i.e., S-basis constraint. Based on the S-basis, the types of rank deficiency and their S-basis constraints can be found in Table 1. It should be noted that this choice of S-basis holds for the Code Division Multiple Access (CDMA) signals, and different choice of S-basis should be applied for the Frequency Division Multiple Access (FDMA) signals (Zhang et al., 2021).

In Table 1, p and q denote the reference receiver and satellite, respectively. In addition, B_{IF}^s, B_{GF}^s, $B_{r,\mathrm{IF}}$ and $B_{r,\mathrm{GF}}$ can be described as:

$$\begin{cases} B_{\mathrm{IF}}^s = \dfrac{\mu_2 B_1^S - \mu_1 B_2^S}{\mu_2 - \mu_1} \\ B_{\mathrm{GF}}^s = \dfrac{B_2^S - B_1^S}{\mu_2 - \mu_1} \\ D_{\mathrm{DCB}}^S = B_2^S - B_1^S \\ B_{\mathrm{IF}}^s = \dfrac{\mu_2 B_{r,1} - \mu_1 B_{r,2}}{\mu_2 - \mu_1} \\ B_{\mathrm{GF}}^s = \dfrac{B_{r,2} - B_{r,1}}{\mu_2 - \mu_1} \\ D_{\mathrm{DCB}}^r = B_{r,2} - B_{r,1} \end{cases} \tag{2}$$

When the rank deficiencies in Eq. (1) are eliminated based on the S-basis listed in Table 1, the full-rank un-differenced and un-combined PPP–RTK network code and phase observations at epoch k can be expressed as:

$$\begin{cases} \mathrm{E}(\Delta P_{r,i}^s(k)) = c \cdot [\overline{\mathrm{d}t}_{r\neq p}(k) - \overline{\mathrm{d}t}^s(k)] + g_r^s \cdot \overline{T}_{r\neq p}^s(k) \\ \qquad\qquad + \mu_i \cdot \overline{I}_{r,i}^s(k) + \overline{B}_{r\neq p,i>2} - \overline{B}_{i>2}^s \\ \mathrm{E}(\Delta \Phi_{r,i}^s(k)) = c \cdot [\overline{\mathrm{d}t}_{r\neq p}(k) - \overline{\mathrm{d}t}^s(k)] + g_r^s \cdot \overline{T}_{r\neq p}^s(k) \\ \qquad\qquad - \mu_i \cdot \overline{I}_{r,i}^s(k) + \overline{b}_{r\neq p,i>2} - \overline{b}_i^s + \lambda_i \cdot N_{r\neq p,i}^{s\neq q} \end{cases} \tag{3}$$

The formulations of the estimable parameters in Eq. (3) can be found in Table 2.

As is shown in Table 2, the ionospheric parameters are biased by Geometry-Free (GF) receiver and satellite code biases. These biases are also contained in the interpolated ionospheric delays that are provided to users. As a result,

Table 2 The estimable parameters of un-differenced and un-combined PPP–RTK and corresponding formulations

Parameter	Formulation
$\overline{\mathrm{d}t}^s$	$\mathrm{d}t^s - \mathrm{d}t_p + [B_{\mathrm{IF}}^S - B_{p,\mathrm{IF}} - g_r^s \cdot T_p^s]/c$
$\overline{B}_{i>2}^s$	$B_i^S - B_{\mathrm{IF}}^S - \mu_i B_{\mathrm{GF}}^S - B_{p,i} - B_{p,\mathrm{IF}} + \mu_i B_{p,\mathrm{GF}}$
$\overline{b}_i^s$	$b_i^S - B_{\mathrm{IF}}^S + \mu_i B_{\mathrm{GF}}^S - b_{p,i} - B_{p,\mathrm{IF}} + \mu_i B_{p,\mathrm{GF}} - \lambda_i N_{p,i}^S$
$N_{r\neq p,i}^{s\neq q}$	$(N_{r,i}^S - N_{p,i}^S) - (N_{r,i}^q - N_{p,i}^q)$
$\overline{T}_{r\neq p}^s$	$T_r^s - T_p^s$
$\overline{\mathrm{d}t}_{r\neq p}$	$\mathrm{d}t^s - \mathrm{d}t_p + [B_{\mathrm{IF}}^S - B_{p,\mathrm{IF}}]/c$
$\overline{B}_{r\neq p,i>2}$	$(B_{r,i} - B_{r,\mathrm{IF}} - \mu_i B_{r,\mathrm{GF}}) - (B_{p,i} - B_{p,\mathrm{IF}} - \mu_i B_{p,\mathrm{GF}})$
$\overline{b}_{r\neq p,i>2}$	$(b_{r,i} - B_{r,\mathrm{IF}} + \mu_i B_{r,\mathrm{GF}} + \lambda_i N_{r,i}^q) - (b_{p,i} - B_{p,\mathrm{IF}} + \mu_i B_{p,\mathrm{GF}} + \lambda_i N_{p,i}^q)$
$\overline{I}_{r,i}^s$	$I_r^s + B_{r,\mathrm{GF}} - B_{\mathrm{GF}}^S$

Table 3 The estimable formulation for the un-differenced and un-combined PPP–RTK sever model

Parameter	Formulation
$\overline{B}_{r\neq p,\mathrm{DCB}}$	$B_{r,\mathrm{DCB}} - B_{p,\mathrm{DCB}}$
$\overline{b}_{r\neq p,i>2}$	$(b_{r,i} - B_{r,\mathrm{IF}} + \lambda_i N^q_{r,i}) - (b_{p,i} - B_{p,\mathrm{IF}} + \lambda_i N^q_{p,i})$
$\overline{I}^s_{r,i}$	$I^s_r + B_{r,\mathrm{GF}} - B^S_{\mathrm{GF}}$

the interpolated user ionospheric delay for different satellites will contain different combinations of receiver code biases when the different receivers of a network observe different satellites, resulting in system biases for PPP–RTK users of the network. It is worth noting that the system biases can be eliminated by single differencing between satellites when the ionospheric delays are used as constraints in PPP–RTK.

It should be mentioned that Eq. (3) ignores the spatial correlation of ionospheric delays in the network. The slant ionospheric delays derived from the network receivers for the same satellite are approximately equal if the distances between the receivers are a few hundred kilometers (Odijk, 2002). Accordingly, the redundant observation equation, i.e., the single-differenced ionospheric code observations described in Eq. (4), can be added to Eq. (1).

$$I^s_p(k) - I^s_{r\neq p}(k) = 0,\ W = S^{-1} \tag{4}$$

where W and S denote the weight and variance–covariance matrix of the single-differenced ionospheric code observations between receivers.

Once the single differenced ionospheric code observations between receivers are added to Eq. (1), it will not be a rank deficiency system. After eliminating the rank deficiency, the full rank un-differenced and un-combined PPP–RTK can be formulated as:

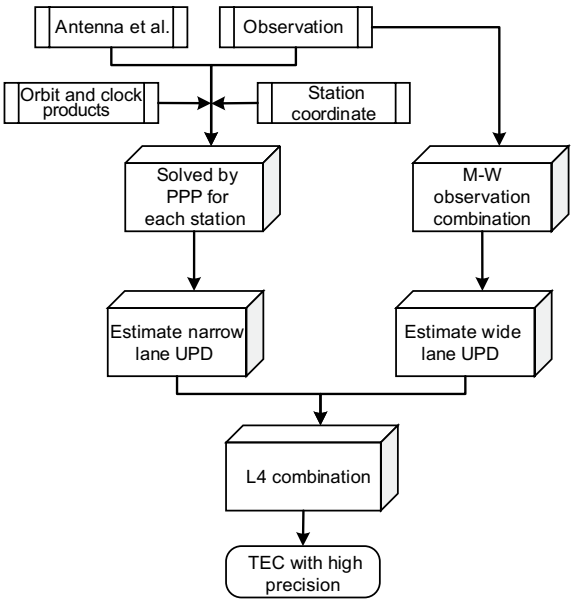

Fig. 1 Flow chart of ionospheric delay estimated by using the PPP-Fixed method

where the estimable forms of the biased receiver code biases, phase biases, and ionospheric delays are listed in Table 3.

It can be seen from Table 3 that the estimable ionospheric parameters of the network reference receiver include GF receiver code biases. Therefore, the interpolated ionospheric delays provided to users contain the same receiver Differential Code Bias (DCB), which is eventually absorbed by the estimated receiver code and phase bias of users.

Precise ionospheric delay estimation

As is mentioned above, the convergence time can be reduced by applying the constraint of ionospheric

$$\begin{cases} \mathrm{E}(\Delta P^s_{r,i}(k)) = c\cdot[\overline{\mathrm{d}t}_{r\neq p}(k) - \overline{\mathrm{d}t}^s(k)] + g^s_r\cdot\overline{T}^s_{r\neq p}(k) \\ \qquad\qquad + \mu_i\cdot\overline{I}^s_{r,i}(k) + \overline{B}_{r\neq p,i>2} - \overline{B}^s_{i>2} + \dfrac{\mu_i}{\mu_2-\mu_1}\overline{B}_{r\neq p,\mathrm{DCB}} \\ \mathrm{E}(\Delta\Phi^s_{r,i}(k)) = c\cdot[\overline{\mathrm{d}t}_{r\neq p}(k) - \overline{\mathrm{d}t}^s(k)] + g^s_r\cdot\overline{T}^s_{r\neq p}(k) \\ \qquad\qquad - \mu_i\cdot\overline{I}^s_{r,i}(k) + \overline{b}_{r\neq p,i>2} - \overline{b}^s_i + \lambda_i\cdot N^{s\neq q}_{r\neq p,i} \\ \overline{I}^s_r - \overline{I}^s_{r\neq p} = 0 \end{cases} \tag{5}$$

information, which can be derived from GF combination. In recent decades, three methods were used for the extraction of ionospheric observables, such as the Carrier-to-Code Levelling (CCL) method (Ciraolo et al., 2007), the un-differenced and un-combined PPP (UD-PPP) method (Zhang et al., 2012), and the zero-difference integer ambiguity (PPP-Fixed) method (Ren et al., 2020). The CCL method only considers the noise of a specific satellite in a continuous arc, leading to large errors between different satellites when the reference of each satellite is different. The UD-PPP method uses external constraints and performs the adjustment of the selected network by the least-squares method. The estimated ambiguity can be the best for the satellites tracked by a certain receiver, and the differences between different satellites can be effectively reduced. In addition to the advantages of the UD-PPP, the PPP-Fixed fully utilizes the constraints of receivers for the whole network. Furthermore, ionospheric observables extracted from carrier phase observations by using the PPP-Fixed method have higher accuracy than those extracted with CCL and UD-PPP. The PPP-Fixed method is applied for ionospheric delay extraction. The processing flow chart of this method is plotted in Fig. 1 and its detailed processing steps can be found in (Ren et al., 2020).

PPP–RTK user model

The receiver of a user can be theoretically regarded as a part of network. Therefore, the rank deficiencies and corresponding S-basis for users are nearly the same as those of network receivers. Unlikely, the positions of users need to be estimated and the $\overline{\mathrm{d}t}^s$, $\overline{B}^s_{i>2}$, and $\overline{b}^s_i$ need to be corrected as well. Therefore, the PPP–RTK user model is given as follows:

$$\begin{cases} E(\Delta P^s_{r,i}(k) + c\cdot\overline{\mathrm{d}t}^s(k) + \overline{\mathrm{d}t}^S_{j>2}(k)) \\ \quad = c^S_u(k)\cdot\Delta x_u(k) + c\cdot\widehat{\mathrm{d}t}_u(k) + g^s_u\cdot\widehat{T}^s_u(k) + \mu_i\cdot\widehat{I}^s_u(k) + \overline{B}_{u,i>2} + \mu_i\cdot\widehat{B}_{u,\mathrm{GF}} \\ E(\Delta\Phi^s_{r,i}(k) + c\cdot\overline{\mathrm{d}t}^s(k) + b^S_{j>2}(k)) \\ \quad = c^S_u(k)\cdot\Delta x_u(k) + c\cdot\widehat{\mathrm{d}t}_u(k) + g^s_u\cdot\widehat{T}^s_u(k) - \mu_i\cdot\widehat{I}^s_u(k) + \widehat{b}_{u,i>2} + \lambda_i\cdot N^{s\neq q}_{u,i} \\ \overline{I}^s_{\mathrm{Interpolate}} = \overline{I}^s_{r\neq p} \end{cases} \tag{6}$$

Table 4 The estimable parameters for a PPP–RTK user

Parameter	Formulation
$\widehat{B}_{u,\mathrm{GF}}$	$B_{u,\mathrm{GF}} - B_{p,\mathrm{GF}}$
$\widehat{I}^s_u$	$I^s_u + B_{p,\mathrm{GF}} - B^S_{\mathrm{GF}}$
$b_{u,i}$	$(b_{u,i} - B_{u,\mathrm{IF}} + \lambda_i N^q_{u,i}) - (b_{p,i} - B_{p,\mathrm{IF}} + \lambda_i N^q_{p,i})$

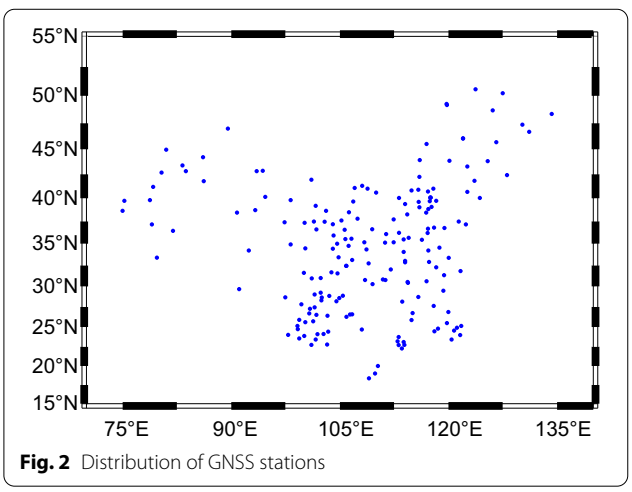

Fig. 2 Distribution of GNSS stations

where the formulations of the estimable parameter are listed in Table 4. When the ionospheric delays provided to users are interpolated by network ionospheric delays, Eq. (6) represents the PPP–RTK user model, and $\widehat{B}_{u,\mathrm{GF}}$ needs to be estimated. It should be noted that the ionospheric delay corrections contribute to the rapid convergence at the beginning significantly when a new satellite is observed, or outages occur.

Results and discussion

In this section we first describe the performances of the PPP–RTK constrained by the external ionospheric information derived from different types of networks. Then we analyze the dependencies of convergence time on the prior variances of the ionospheric delays. Finally, a Travelling Ionospheric Disturbance (TID) is simulated and its impacts on the PPP–RTK performances are presented. For PPP–RTK test, the data collected by about 190 GNSS stations from 2020/04/01 to 2020/04/08 are applied. The distribution of GNSS stations, which are mainly located in the Chinese mainland, is plotted in Fig. 2.

The parameter estimation is performed by the least square method for the network, while the Kalman filter and kinematic mode are applied for users. The satellite with the maximum elevation angle for a specific epoch is selected as a reference. The satellite positions and satellite

Table 5 The detailed processing setups for PPP–RTK

Item	Strategy
Float PPP	Global Positioning System (GPS), GLObal NAvigation Satellite System (GLONASS), Galileo navigation satellite system (Galileo) and BeiDou navigation satellite system (BDS)
Ambiguity fixed	GPS
Frequency	L1 and L2
Weight strategy	Elevation dependent
Priori precision	0.3 m for code observation 0.03 m for phase observation
Tropospheric delay	Without external tropospheric information constraints Saastamoinen model (Saastamoinen, 1972) for hydrostatic component Estimated as random walk for zenith total tropospheric delay Global Mapping Function (GMF) (Boehm et al., 2006) is used as tropospheric mapping function
Ionospheric delay	With external ionospheric information constraints Server: zero-differenced integer ambiguity fixed method Users: constrained by network corrections using inversed distance weight
Elevation cutoff	10°
Satellite DCB	Corrected with the monthly satellite DCB products provided by CODE

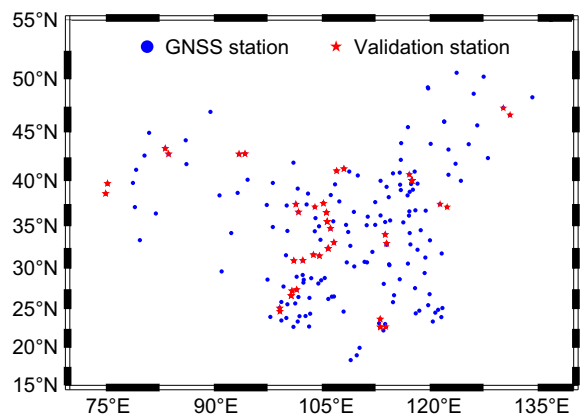

Fig. 3 Distribution of GNSS stations and validation stations for a regional network

clock errors are derived from the precise satellite orbit and clock products provided by the International GNSS Service (IGS). The receiver positions of the network are fixed to their known values. The code and phase biases of receivers and satellites are treated as time-invariant parameters. Other kinds of error sources in positioning, such as the solid earth tide, the ocean tide, the relativistic effects, as well as satellite receiver Phase Center Offset (PCO) and Phase Center Variation (PCV), are corrected by corresponding models. The ambiguity term of the reference station is fixed by estimating the Un-calibrated Phase Delays (UPD). In this study, the UPDs are estimated by using the method introduced by Li & Zhang (2012). The ambiguities of users are resolved by using the Least-squares AMBiguity Decorrelation Adjustment (LAMBDA) method (Teunissen, 1995). Other main processing strategies are listed in Table 5.

PPP–RTK test for different network scales

In PPP–RTK processing, the Kalman filter is reinitialized every hour.

Figure 3 presents the distribution of GNSS stations and validation stations, which are applied for the regional network test of the PPP–RTK constrained by interpolated ionospheric delays.

Figure 4 illustrates the performance comparisons of the PPP-AR and the PPP–RTK constrained by Global Ionosphere Map (PPP–RTK-GIM). As we can see, The Time to First Fix (TTFF) of PPP–RTK-GIM for different IGS stations is improved by 20%-50% as compared with that of PPP-AR.

To better understand how the ionospheric delays derived from different network scales affect the performances of a PPP–RTK user, the small-scale (about 300 km), medium-scale (about 500 km) and large-scale (800 km) networks are designed and shown in Fig. 5. The number of reference stations is about 80, 40, and 30 for small-scale, medium-scale, and large-scale networks, respectively. Both small-scale and medium-scale networks consider the spatial variations of the ionosphere and the distribution of GNSS stations, while the distances between the reference stations for small-scale network are smaller than those for medium-scale network. The large-scale network contains less reference stations that can nearly cover China, leading to the longest distances between reference stations. Hence,

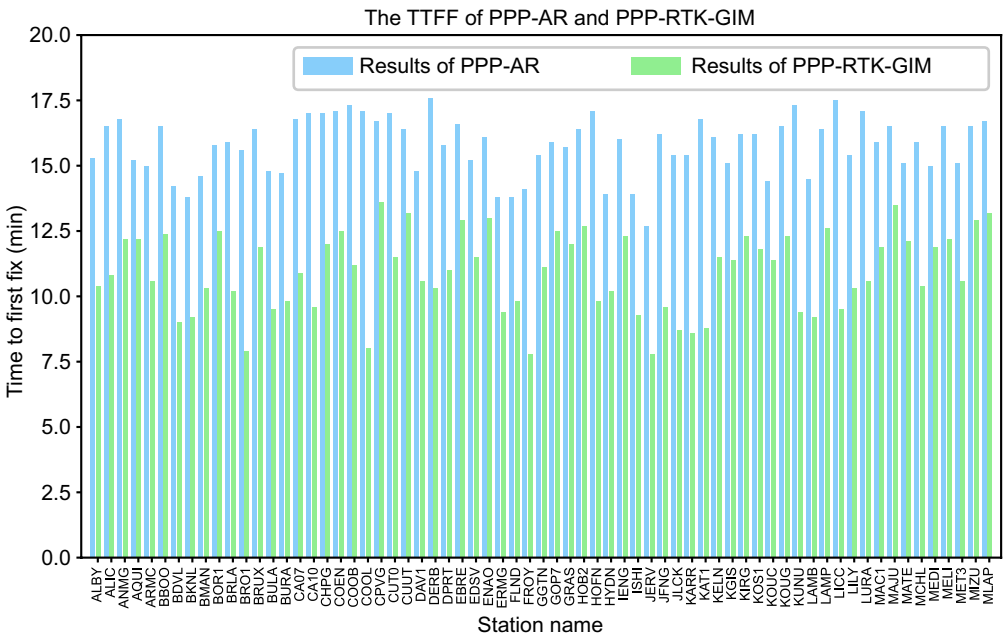

Fig. 4 Statistical results of PPP-AR and PPP–RTK constrained by GIM

the large-scale network considers neither the spatial variations of the ionosphere nor the distribution of available reference stations.

Figure 6 compares the statistical results of TTFF and fixing rate for the PPP–RTK constrained by the ionospheric delays interpolated from small-scale, medium-scale, and large-scale networks, denoted as PPP–RTK-300, PPP–RTK-500, and PPP–RTK-800, respectively. From Fig. 6 we can see that PPP–RTK-300 performs best, followed by PPP–RTK-500, and then PPP–RTK-800. This is due to the fact that the spatial variation of the ionosphere depends much on the distance between stations. The TTFF is about 4.4, 5.2, and 6.8 min for the PPP–RTK-300, PPP–RTK-500, and PPP–RTK-800, respectively. And their corresponding fixing rate is 97%, 96%, and 93%, respectively.

The relationship between convergence time and different prior variances

The above results indicate that the TTFF can be reduced for the PPP–RTK constrained by ionospheric delay. However, due to the large number of the stations and long data length in the test, we could not determine the optimum variance to test them one by one. To figure out the relationship between the variance of the given ionospheric delay corrections and the convergence time of PPP–RTK, we added the random errors to the provided ionospheric delay corrections as follows:

$$\tilde{I}^s_{r,\mathrm{bias}} = \tilde{I}^s_r + \sigma \tag{7}$$

where σ denotes the random error. In order to avoid the added random error close to zero, the random error should meet the following condition:

$$0.5 \times S^{\mathrm{Error}}_{\mathrm{Max}} \le |\sigma| \le S^{\mathrm{Error}}_{\mathrm{Max}} \tag{8}$$

where $S^{\mathrm{Error}}_{\mathrm{Max}}$ expresses the threshold value of the added error.

Figure 7 presents the convergence time for different errors of less than 0.5 TECU, 1 TECU, 3 TECU and 5 TECU that are added to the network-derived ionospheric delays with optimum variances. As is shown in Fig. 7, all the positioning accuracy better than 10 cm can be achieved within 7 min. Although the variance can properly describe the accuracy of ionospheric delay, the convergence time increases with the increase of added ionospheric errors. The convergence time is about 3, 5, and 6 min, respectively, when the corresponding added error is about 1 TECU, 3 TECU, and 5 TECU with optimum variance. Meanwhile, the convergence time is less than 1 min when the added error of ionospheric delay is smaller than 0.5 TECU with optimum variance.

Figure 8 illustrates the convergence time of PPP-AR and that of the PPP–RTK constrained by ionospheric delay corrections with an error of 3 TECU for different variances. It shows that the variances of ionospheric

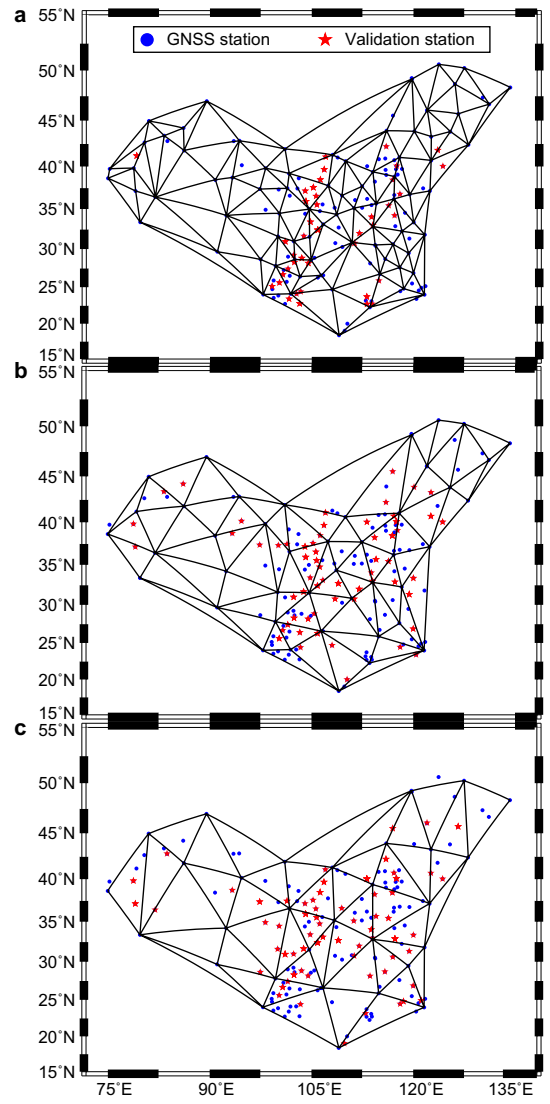

Fig. 5 The designed networks with point spacing of **a** 300, **b** 500, and **c** 800 km

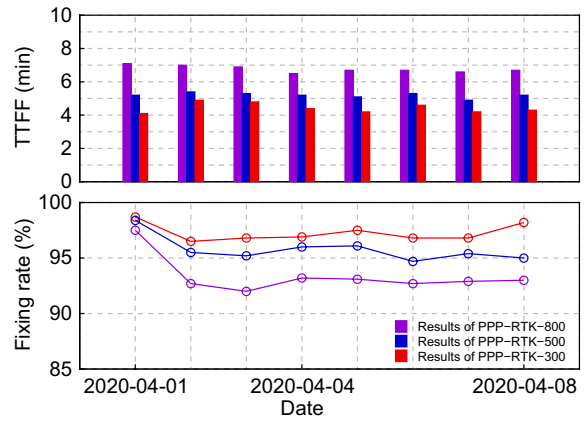

Fig. 6 Statistical results of the PPP–RTK constrained by the ionospheric delays interpolated from different scales of network

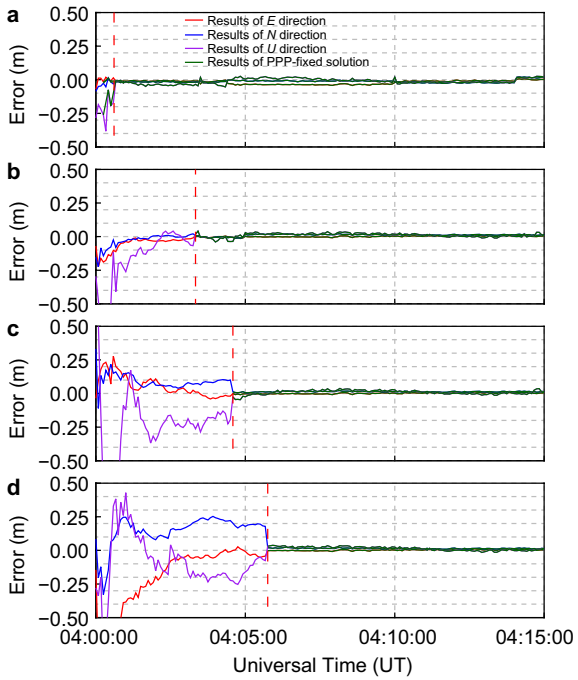

Fig. 7 The convergence time of the ionospheric delay corrections with an error of **a** smaller than 0.5 TECU, **b** 1 TECU, **c** 3 TECU, and **d** 5 TECU as optimum variance, respectively

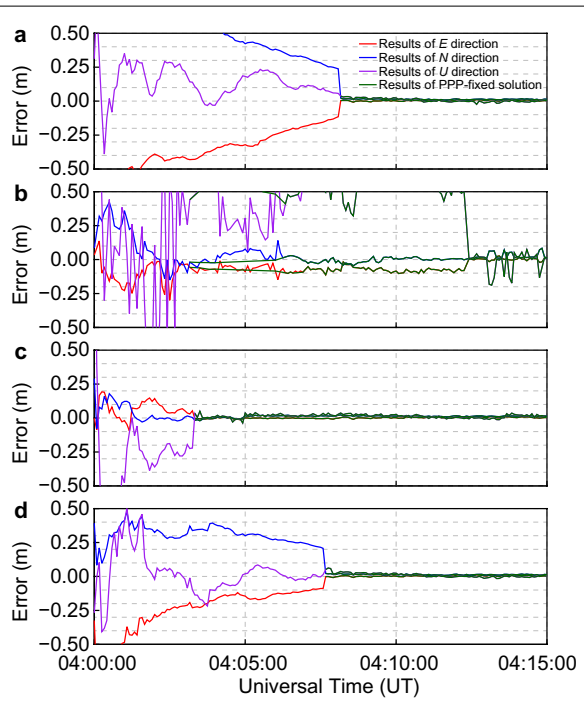

Fig. 8 The convergence time of **a** PPP-AR, and the ionospheric delay corrections with an error of 3 TECU while **b** the variance is very small (< 1 TECU), **c** the variance is the optimum (= 3 TECU), and **d** the variance is large (> 5TECU)

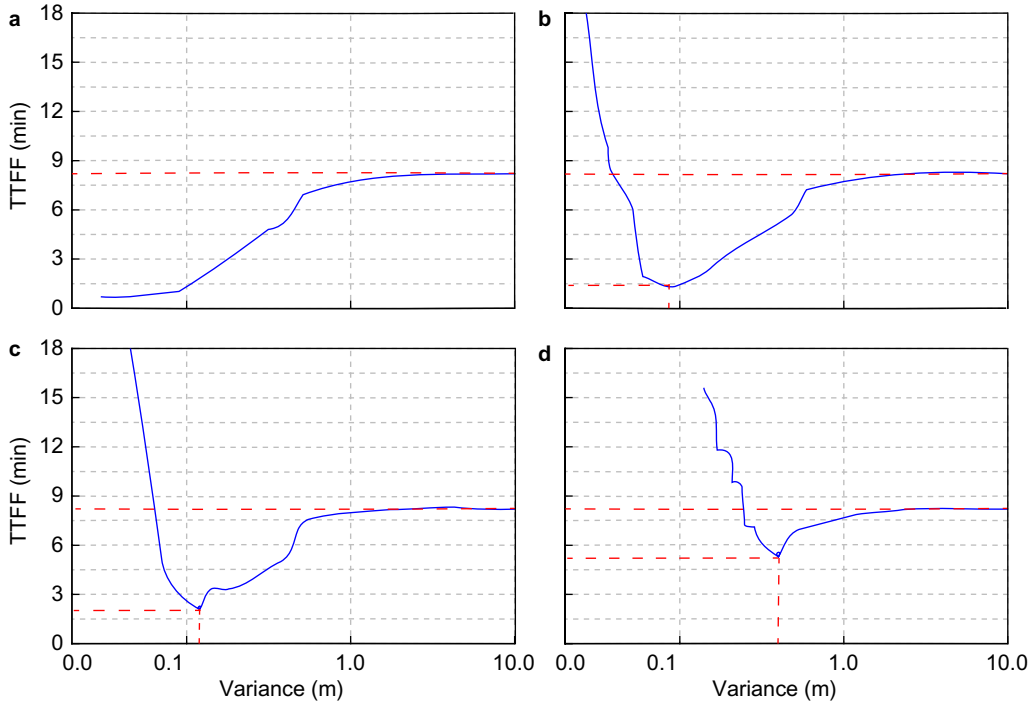

Fig. 9 The convergence time of the PPP–RTK constrained by external ionospheric delay information with an error of **a** 0, **b** 1 TECU, **c** 3 TECU, and **d** 5 TECU for different variances

delay corrections affect the convergence time significantly. On the one hand, a very small variance of the ionospheric delay with an error of 3 TECU leads to the lower fixing rate and a longer convergence time compared with those of PPP-AR. Meanwhile, the stability and reliability of the positioning errors during the un-convergence period are not ideal. On the other hand, when the variance of ionospheric delay correction is too large, the convergence time of the PPP–RTK constrained by ionospheric delay corrections is nearly the same as that

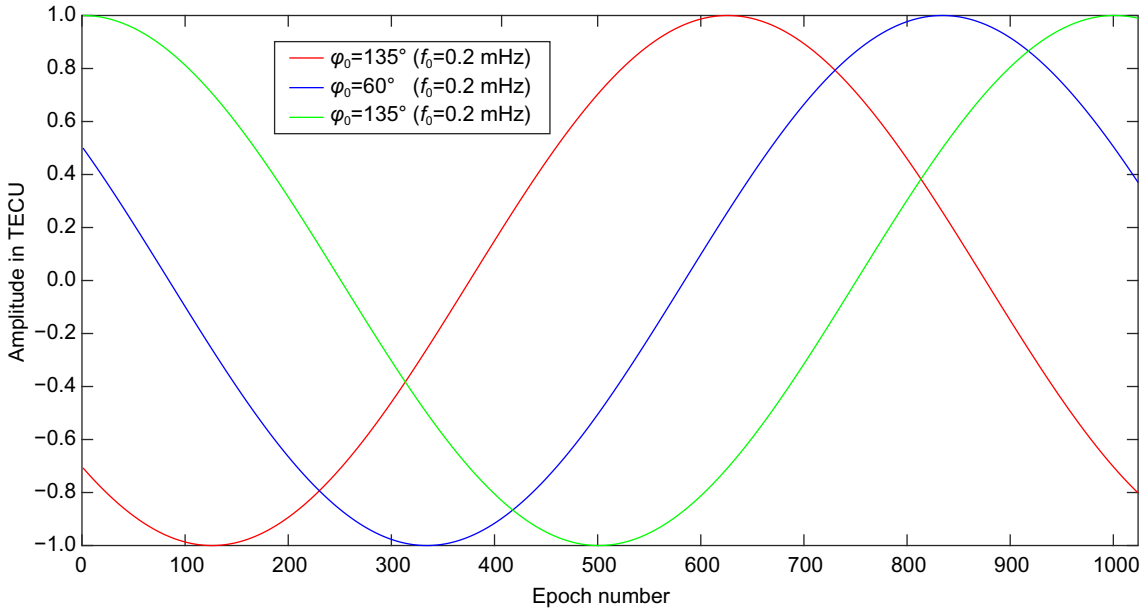

Fig. 10 The simulation results of TID with same direct component, amplitude, and frequency but different initial phases

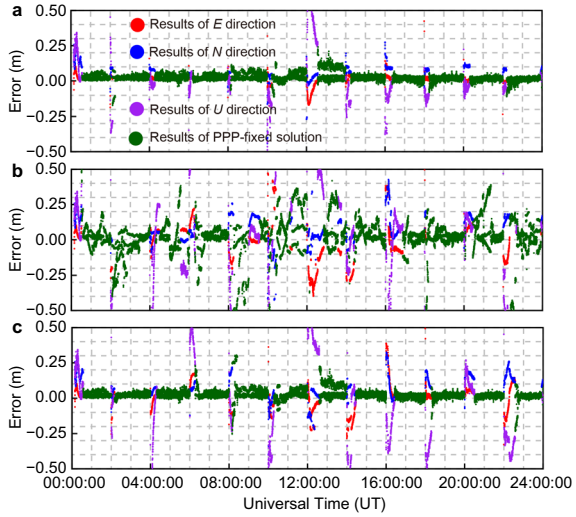

Fig. 11 The convergence time of PPP–RTK constrained by ionospheric delay corrections with **a** no TID, and with a TID of an amplitude of 1 TECU and the variance of **b** 0.088 m, and **c** 0.38 m

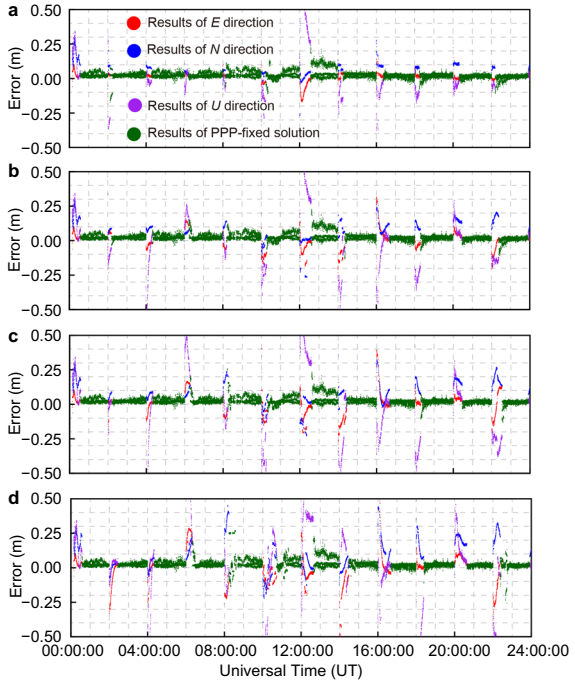

Fig. 12 The convergence time of the PPP–RTK constrained by external ionospheric information with **a** no TID, and with TID of the amplitude for **b** 0.5 TECU, **c** 1 TECU, and **d** 2 TECU and the variance of 0.48 m

of PPP-AR, but the positioning accuracy during the unconvergence period is better than that of PPP-AR. When the variance matches the accuracy of ionospheric delay corrections, the convergence time of the PPP–RTK constrained by ionospheric delay corrections can be reduced significantly compared with that of PPP-AR.

Figure 9 describes the convergence time for the different errors of ionospheric delay corrections with different variances. As shown in Fig. 9, the convergence time varies similarly for the different errors of ionospheric delay corrections. Generally, the convergence time is long when the variance is very small, while the convergence time is almost the same as that of PPP-AR when the variance is large. The convergence time will be reduced significantly if the variance can best match the accuracy of the ionospheric delay corrections when compared with that of PPP-AR. In terms of the ionospheric delay corrections without errors, the convergence time will be the same as that of PPP-AR if the variance is large enough, and the convergence time will be very short if the variance is very small.

The performance of PPP–RTK during the periods of ionospheric disturbances

Travelling Ionospheric Disturbance (TID) is the ionospheric density fluctuation that propagates as a wave through the ionosphere at a wide range of velocities and frequencies (Belehaki et al., 2020; Saito et al., 1998; Tsugawa et al., 2004, 2007). The high occurrence rate of TIDs and complicated variety of their characteristics regarding their velocity, propagation direction, and amplitude impact the operation of ground-based infrastructures, especially real-time kinematic services, and radio communication (Hernández-Pajares et al., 2006, 2012). In this study, a TID is simulated and its impacts on the convergence time of the PPP–RTK constrained by external ionospheric delay information are analyzed. For this purpose, the simulated TID can be expressed as follows:

$$S = A_0 + A_1 \cdot \cos(2 \cdot \pi \cdot f_0 \cdot t + \varphi_0) \tag{9}$$

where S indicates the simulated results; A_0 expresses the direct component in TECU; A_1 is the amplitude of the TID in TECU; f_0 is the frequency of the TID in Hz; t is the number of epoch; φ_0 denotes the initial phase of the TID with an unit of rad. Suppose that $A_0 = 0$, $A_1 = 1$, and $f_0 = 0.2$ mHz, the simulated TIDs with different initial phases are shown in Fig. 10.

To study the impacts of TID on PPP–RTK, the TID is firstly simulated by assuming that $A_0 = 0$, $A_1 = 1$, $f_0 = 0.2$ mHz and φ_0=135°. Then the TID errors are added to the ionospheric delay corrections. The convergence time of the PPP–RTK constrained by ionospheric delay corrections with a best variance and influenced by TID errors for different variances can be found in Fig. 11. As can be seen from Fig. 11, the positioning results of

PPP–RTK are poor due to the influence of TID. Moreover, the convergence time and reliability are affected as well, which is mainly related to the prior variance of the ionospheric delay. Particularly, if the same variance is adopted after adding TID errors with that during the durations without the TID errors, the positioning errors will be very large and vary greatly. The positioning accuracy is always larger than 10 cm and there are some situations where the ambiguities are wrongly fixed. In addition, much longer convergence time is needed during the TID period if the prior variance is larger. The positioning errors will be smaller than 10 cm after convergence, but still worse than that without adding TID errors.

Furthermore, TIDs are simulated with $A_0 = 0$, $f_0 = 0.2$ mHz and φ_0=135°, but with different amplitudes. The convergence time with the same variances for PPP–RTK during the TID periods are investigated and the results are plotted in Fig. 12. As we can see, the impacts of TIDs increase as the amplitudes of TIDs become larger. Note that the impact of TIDs is more significant at the beginning of convergence for each reinitialized period. When the ambiguity parameter is fixed, the positioning errors are nearly the same as those of the case without TIDs. Meanwhile, the convergence time will be longer for the TIDs with the larger amplitudes.

Conclusions

In this study, the relationship between the accuracy of ionospheric delay corrections and the convergence time is investigated. The PPP–RTK network model, PPP–RTK user model, and the method to extract ionospheric delay are first described. Then, the positioning performances of the PPP–RTK constrained by ionospheric delay with different errors, and with different TID situations are presented. The results of this study are summarized as follows.

(1) In terms of the TTFF for PPP-AR and PPP–RTK-GIM, the performance of the PPP–RTK constrained by global ionosphere maps can be improved compared with that of PPP-AR. The TTFF is about 8–10 min and 13–16 min for PPP-AR and PPP–RTK-GIM, respectively. The improvement of TTFF for the PPP–RTK-GIM is about 20% ~ 50%.
(2) The errors of 0.5 TECU, 1 TECU, 3 TECU and 5 TECU are added to the network-derived ionospheric delays, respectively, which are used to constrain PPP–RTK with optimum variances. The results show that all the positioning errors smaller than 10 cm can be achieved within 7 min and the convergence time depends on the accuracy of ionospheric delay corrections. The convergence time is about 3, 5, and 6 min, respectively, when the added errors are about 1, 3, and 5 TECU with optimum variance, while it is about 1 min for the error less than 0.5 TECU. In addition, the convergence time of the PPP–RTK constrained by ionospheric delay with an error of 3 TECU for different variances is investigated. The results indicate that the variance of ionospheric delay affects the convergence time significantly. The convergence time for the ionospheric delay with errors have the similar variation. The convergence time will be very long when the variance is very small, while it will be the same as that of PPP-AR when the variance is very large.
(3) Finally, the impacts of TID on the convergence time of PPP–RTK are checked by a simulation. The TID can affect the convergence time, positioning accuracy and reliability of PPP–RTK, which are related to the given variances. In addition, the larger variance leads to a longer time of convergence and the impact of TID will be enhanced with the increase of TID amplitude.

Acknowledgements
The numerical calculations have been done on the supercomputing system in the Supercomputing Center of Wuhan University. We also gratefully acknowledge the use of Generic Mapping Tool (GMT) software.

Authors' contributions
Xiaohong Zhang and Xiaodong Ren proposed the idea and drafted the article; Jun Chen and Dengkui Mei carried out the simulation and the evaluation in data analysis; Xiang Zuo and Wanke Liu assisted in article revision. All authors read and approved the final manuscript.

Funding
This work was funded by the National Science Fund for Distinguished Young Scholars (no. 41825009), Changjiang Scholars Program, the National Natural Science Foundation of China (No.42174031, 41904026), the Technology Innovation Special Project (Major program) of Hubei Province of China (No. 2019AAA043), and initial scientific research fund of talents in Minjiang University (No. MJY21039).

Availability of data and material
Not applicable.

Declarations

Competing interests
The authors declare that they have no competing interests.

Author details
[1]Chinese Antarctic Center of Surveying and Mapping, Wuhan University, Wuhan 430079, China. [2]School of Geodesy and Geomatics, Wuhan University, Wuhan 430079, China. [3]Department of Surveying and Mapping Engineering, Minjiang University, Fuzhou 350118, China. [4]Department of Geodesy, GeoForschungsZentrum (GFZ), Telegrafenberg, 14473 Potsdam, Germany.

Received: 20 December 2021 Accepted: 28 February 2022
Published online: 28 March 2022

References

Banville, S., Collins, P., Zhang, W., & Langley, R. B. (2014). Global and Regional Ionospheric Corrections for Faster PPP Convergence. *Navigation, 61*, 115–124. https://doi.org/10.1002/navi.57

Belehaki, A., Tsagouri, I., Altadill, D., Blanch, E., Borries, C., Buresova, D., Chum, J., Galkin, I., Juan, J. M., Segarra, A., Timoté, C. C., Tziotziou, K., Verhulst, T. G. W., & Watermann, J. (2020). An overview of methodologies for real-time detection, characterisation and tracking of traveling ionospheric disturbances developed in the TechTIDE project. *Journal Space Weather Space Climate, 10*, 42.

Boehm, J., Niell, A., Tregoning, P., & Schuh, H. (2006). Global mapping function (GMF): A new empirical mapping function based on numerical weather model data. *Geophysical Research Letters*. https://doi.org/10.1029/2005GL025546

Ciraolo, L., Azpilicueta, F., Brunini, C., Meza, A., & Radicella, S. M. (2007). Calibration errors on experimental slant total electron content (TEC) determined with GPS. *Journal of Geodesy, 81*, 111–120. https://doi.org/10.1007/s00190-006-0093-1

Collins, P., Lahaye, F., Héroux, P., & Bisnath, S. (2008). Precise point positioning with ambiguity resolution using the decoupled clock model. 21st International Technical Meeting of the Satellite Division of the Institute of Navigation, ION GNSS 2008*,* 3, 1549–1556.

De Oliveira, P. S., Morel, L., Fund, F., Legros, R., Monico, J. F. G., Durand, S., & Durand, F. (2017). Modeling tropospheric wet delays with dense and sparse network configurations for PPP–RTK. *GPS Solutions, 21*, 237–250. https://doi.org/10.1007/s10291-016-0518-0

Wen,D., Zhang, X.,Tong,Y., Zhang,G.,Zhang, M.,&Leng,R.(2015). GPS-based ionospheric tomography with a constrained adaptive simultaneous algebraic reconstruction technique. Journal of earth system science, 124(2), 283-289.https://doi.org/10.1007/s12040-015-0542-4

Ge, M., Gendt, G., Rothacher, M., Shi, C., & Liu, J. (2008). Resolution of GPS carrier-phase ambiguities in Precise Point Positioning (PPP) with daily observations. *Journal of Geodesy, 82*, 389–399. https://doi.org/10.1007/s00190-007-0187-4

Geng, J., & Shi, C. (2017). Rapid initialization of real-time PPP by resolving undifferenced GPS and GLONASS ambiguities simultaneously. *Journal of Geodesy, 91*, 361–374. https://doi.org/10.1007/s00190-016-0969-7

Geng, J., Li, X., Zhao, Q., et al. (2019). Inter-system PPP ambiguity resolution between GPS and BeiDou for rapid initialization. *Journal of Geodesy, 93*(3), 383–398.

Geng, J., Meng, X., Dodson, A., et al. (2010). Rapid re-convergences to ambiguity-fixed solutions in precise point positioning. *Journal of Geodesy, 84*, 705–714. https://doi.org/10.1007/s00190-010-0404-4

Guo, F., Li, X., Zhang, X., & Wang, J. (2017). The contribution of Multi-GNSS Experiment (MGEX) to precise point positioning. *Advances in Space Research, 59*, 2714–2725. https://doi.org/10.1016/j.asr.2016.05.018

Haines, G. V. (1988). Computer programs for spherical cap harmonic analysis of potential and general fields. *Computers & Geosciences, 14*, 413–447. https://doi.org/10.1016/0098-3004(88)90027-1

Hernández-Pajares, M., Juan, J. M., & Sanz, J. (1999). New approaches in global ionospheric determination using ground GPS data. *Journal of Atmospheric and Solar-Terrestrial Physics, 61*, 1237–1247. https://doi.org/10.1016/S1364-6826(99)00054-1

Hernández-Pajares, M., Juan, J. M., & Sanz, J. (2006). Medium-scale traveling ionospheric disturbances affecting GPS measurements: Spatial and temporal analysis. *Journal of Geophysical Research: Space Physics*. https://doi.org/10.1029/2005JA011474

Hernández-Pajares, M., Juan, J. M., Sanz, J., & Aragón-Àngel, A. (2012). Propagation of medium scale traveling ionospheric disturbances at different latitudes and solar cycle conditions. *Radio Science, 47*, 1–22. https://doi.org/10.1029/2011RS004951

Hernández-Pajares, M., Juan, J. M., Sanz, J., Aragón-Àngel, À., García-Rigo, A., Salazar, D., & Escudero, M. (2011). The ionosphere: Effects, GPS modeling and the benefits for space geodetic techniques. *Journal of Geodesy, 85*, 887–907. https://doi.org/10.1007/s00190-011-0508-5

Hu, J., Zhang, X., Li, P., Ma, F., & Pan, L. (2019). Multi-GNSS fractional cycle bias products generation for GNSS ambiguity-fixed PPP at Wuhan University. *GPS Solutions, 24*, 15. https://doi.org/10.1007/s10291-019-0929-9

Jakowski, N., Mayer, C., Wilken, V., & Hoque, M. M. (2008). Ionospheric impact on GNSS signals. *Física De La Tierra, 20*, 11.

Laurichesse, D., Mercier, F., Berthias, J. P., Broca, P., & Cerri, L. (2009). Integer ambiguity resolution on undifferenced GPS phase measurements and its application to PPP and satellite precise orbit determination. *Navigation, 56*, 135–149.

Li, P., Zhang, X., Ren, X., Zuo, X., & Pan, Y. (2016). Generating GPS satellite fractional cycle bias for ambiguity-fixed precise point positioning. *GPS Solutions, 20*, 771–782. https://doi.org/10.1007/s10291-015-0483-z

Li, X., Ge, M., Dai, X., Ren, X., Fritsche, M., Wickert, J., & Schuh, H. (2015a). Accuracy and reliability of multi-GNSS real-time precise positioning: GPS, GLONASS, BeiDou, and Galileo. *Journal of Geodesy, 89*, 607–635. https://doi.org/10.1007/s00190-015-0802-8

Li, X., Li, X., Liu, G., Feng, G., Yuan, Y., Zhang, K., & Ren, X. (2019a). Triple-frequency PPP ambiguity resolution with multi-constellation GNSS: BDS and Galileo. *Journal of Geodesy, 93*, 1105–1122. https://doi.org/10.1007/s00190-019-01229-x

Li, X., Li, X., Ma, F., Yuan, Y., Zhang, K., Zhou, F., & Zhang, X. (2019b). Improved PPP Ambiguity Resolution with the Assistance of Multiple LEO Constellations and Signals. *Remote Sensing, 11*, 408.

Li, X., Ma, F., Li, X., Lv, H., Bian, L., Jiang, Z., & Zhang, X. (2019c). LEO constellation-augmented multi-GNSS for rapid PPP convergence. *Journal of Geodesy, 93*, 749–764. https://doi.org/10.1007/s00190-018-1195-2

Li, X., & Zhang, X. (2012). Improving the estimation of uncalibrated fractional phase offsets for PPP ambiguity resolution. *Journal of Navigation, 65*, 513–529. https://doi.org/10.1017/S0373463312000112

Li, X., Zhang, X., & Ge, M. (2011). Regional reference network augmented precise point positioning for instantaneous ambiguity resolution. *Journal of Geodesy, 2011*(85), 151–158. https://doi.org/10.1007/s00190-010-0424-0

Li, Z., Yuan, Y., Wang, N., Hernandez-Pajares, M., & Huo, X. (2015b). SHPTS: Towards a new method for generating precise global ionospheric TEC map based on spherical harmonic and generalized trigonometric series functions. *Journal of Geodesy, 89*, 331–345. https://doi.org/10.1007/s00190-014-0778-9

Liu, Y., Lou, Y., Ye, S., Zhang, R., Song, W., Zhang, X., & Li, Q. (2017). Assessment of PPP integer ambiguity resolution using GPS, GLONASS and BeiDou (IGSO, MEO) constellations. *GPS Solutions, 21*, 1647–1659. https://doi.org/10.1007/s10291-017-0641-6

Lou, Y., Zheng, F., Gu, S., Wang, C., Guo, H., & Feng, Y. (2016). Multi-GNSS precise point positioning with raw single-frequency and dual-frequency measurement models. *GPS Solutions, 20*, 849–862. https://doi.org/10.1007/s10291-015-0495-8

Mautz, R., Ping, J., Heki, K., Schaffrin, B., Shum, C., & Potts, L. (2005). Efficient spatial and temporal representations of global ionosphere maps over Japan using B-spline wavelets. *Journal of Geodesy, 78*, 662–667. https://doi.org/10.1007/s00190-004-0432-z

Odijk, D. (2002). *Fast precise GPS positioning in the presence of ionospheric delays*. Delft University of Technology.

Odijk, D., Zhang, B., Khodabandeh, A., Odolinski, R., & Teunissen, P. J. G. (2016). On the estimability of parameters in undifferenced, uncombined GNSS network and PPP–RTK user models by means of S-system theory. *Journal of Geodesy, 90*, 15–44. https://doi.org/10.1007/s00190-015-0854-9

Olivares-Pulido, G., Terkildsen, M., Arsov, K., Teunissen, P. J. G., Khodabandeh, A., & Janssen, V. (2019). A 4D tomographic ionospheric model to support PPP–RTK. *Journal of Geodesy, 93*, 1673–1683. https://doi.org/10.1007/s00190-019-01276-4

Psychas, D., Verhagen, S., Liu, X., Memarzadeh, Y., & Visser, H. (2018). Assessment of ionospheric corrections for PPP–RTK using regional ionosphere modelling. *Measurement Science and Technology, 30*, 014001. https://doi.org/10.1088/1361-6501/aaefe5

Ren, X., Chen, J., Li, X., & Zhang, X. (2020). Ionospheric total electron content estimation using GNSS carrier phase observations based on zero-difference integer ambiguity: methodology and assessment. *IEEE Transactions on Geoscience and Remote Sensing*. https://doi.org/10.1109/TGRS.2020.2989131

Saastamoinen, J. (1972). Contributions to the theory of atmospheric refraction. *Bulletin Géodésique, 1946–1975*(105), 279–298. https://doi.org/10.1007/bf02521844

Saito, A., Fukao, S., & Miyazaki, S. (1998). High resolution mapping of TEC perturbations with the GSI GPS Network over Japan. *Geophysical Research Letters, 25*, 3079–3082. https://doi.org/10.1029/98GL52361

Schaer S. (1999). Mapping and predicting the Earth's ionosphere using the Global Positioning System. Unpublished Ph.D Thesis, University of Bern, Bern.
Schmidt, M., Bilitza, D., Shum, C. K., & Zeilhofer, C. (2008). Regional 4-D modeling of the ionospheric electron density. *Advances in Space Research, 42*, 782–790. https://doi.org/10.1016/j.asr.2007.02.050
Teunissen, P., Odijk, D., & Zhang, B. (2010). PPP–RTK: results of CORS network-based PPP with integer ambiguity resolution. *Journal of Aeronautics, Astronautics and Aviation, Series A, 42*, 223–229.
Teunissen, P. J. G. (1995). The least-squares ambiguity decorrelation adjustment: A method for fast GPS integer ambiguity estimation. *Journal of Geodesy, 70*, 65–82. https://doi.org/10.1007/BF00863419
Tsugawa, T., Kotake, N., Otsuka, Y., & Saito, A. (2007). Medium-scale traveling ionospheric disturbances observed by GPS receiver network in Japan: A short review. *GPS Solutions, 11*, 139–144. https://doi.org/10.1007/s10291-006-0045-5
Tsugawa, T., Saito, A., & Otsuka, Y. (2004). A statistical study of large-scale traveling ionospheric disturbances using the GPS network in Japan. *Journal of Geophysical Research: Space Physics*. https://doi.org/10.1029/2003ja010302
Wang, K., Khodabandeh, A., & Teunissen, P. (2017). A study on predicting network corrections in PPP–RTK processing. *Advances in Space Research, 60*, 1463–1477. https://doi.org/10.1016/j.asr.2017.06.043
Wen, D., Yuan, Y., Ou, J., Huo, X., & Zhang, K. (2007). Three-dimensional ionospheric tomography by an improved algebraic reconstruction technique. *GPS Solutions, 11*, 251–258. https://doi.org/10.1007/s10291-007-0055-y
Wen, D., Yuan, Y., Ou, J., Zhang, K., & Liu, K. (2008). A hybrid reconstruction algorithm for 3-D ionospheric tomography. *IEEE Transactions on Geoscience and Remote Sensing, 46*, 1733–1739. https://doi.org/10.1109/TGRS.2008.916466
Wübbena, G., Schmitz, M., Bagge, A. (2005). PPP–RTK: precise point positioning using state-space representation in RTK networks. In *Proceedings of ION GNSS*, pp. 13–16.
Xiang, Y., Gao, Y., & Li, Y. (2020). Reducing convergence time of precise point positioning with ionospheric constraints and receiver differential code bias modeling. *Journal of Geodesy*. https://doi.org/10.1007/s00190-019-01334-x
Zha, J., Zhang, B., Liu, T., & Hou, P. (2021). Ionosphere-weighted undifferenced and uncombined PPP–RTK: Theoretical models and experimental results. *GPS Solution*. https://doi.org/10.1007/s10291-021-01169-0
Zhang, B., Ou, J., Yuan, Y., & Li, Z. (2012). Extraction of line-of-sight ionospheric observables from GPS data using precise point positioning. *Science China Earth Sciences, 55*, 1919–1928. https://doi.org/10.1007/s11430-012-4454-8
Zhang, B., Teunissen, P. J. G., & Odijk, D. (2011). A Novel Un-differenced PPP–RTK Concept. *Journal of Navigation, 64*, S180–S191. https://doi.org/10.1017/s0373463311000361
Zhang, B., Chen, Y., & Yuan, Y. (2018). PPP–RTK based on undifferenced and uncombined observations: Theoretical and practical aspects. *Journal of Geodesy, 93*(7), 1–14.
Zhang, B., Hou, P., Zha, J., & Liu, T. (2021). Integer-estimable FDMA model as an enabler of GLONASS PPP–RTK. *Journal of Geodesy, 95*, 91. https://doi.org/10.1007/s00190-021-01546-0
Zheng, D., Yao, Y., Nie, W., Chu, N., Lin, D., & Ao, M. (2020). A new three-dimensional computerized ionospheric tomography model based on a neural network. *GPS Solutions, 25*, 10. https://doi.org/10.1007/s10291-020-01047-1
Zheng, D., Yao, Y., Nie, W., Liao, M., Liang, J., & Ao, M. (2021). Ordered Subsets-Constrained ART Algorithm for Ionospheric Tomography by Combining VTEC Data. *IEEE Transactions on Geoscience and Remote Sensing, 59*, 7051–7061. https://doi.org/10.1109/TGRS.2020.3029819
Zheng, D., Zheng, H., Wang, Y., Nie, W., Li, C., Ao, M., Hu, W., & Zhou, W. (2017). Variable pixel size ionospheric tomography. *Advances in Space Research, 59*, 2969–2986. https://doi.org/10.1016/j.asr.2017.03.031
Zheng, D. Y., Yao, Y. B., Nie, W. F., Yang, W. T., Hu, W. S., Ao, M. S., & Zheng, H. W. (2018). an improved iterative algorithm for ionospheric tomography reconstruction by using the automatic search technology of relaxation factor. *Radio Science, 53*, 1051–1066. https://doi.org/10.1029/2018rs006588

Publisher's Note